Unraveling the Binding Mechanism of the active form of Remdesivir to RdRp of SARS-CoV-2 and Designing New Potential Analogues: Insights from Molecular Dynamics Simulations

Muhammad Arba[*1], *Nicholas Paradis*[2], *Setyanto T. Wahyudi*[3], *Dylan J. Brunt*[2], *Katherine R. Hausman*[2], *Phillip M. Lakernick*[2], *Mursalin Singh*[2], *and Chun Wu*[2]*

[1]Faculty of Pharmacy, Universitas Halu Oleo, Kendari 93232, Indonesia.

[2]Department of Molecular & Cellular Biosciences, College of Science and Mathematics, Rowan University, Glassboro, New Jersey 08028, United States.

[3]Department of Physics, Faculty of Mathematic and Natural Sciences, IPB University, Bogor 16680, Indonesia.

*To whom correspondence should be addressed: muh.arba@uho.ac.id / wuc@rowan.edu

ABSTRACT: The binding of the active form of Remdesivir (RTP) to RNA-dependent RNA Polymerase (RdRp) of SARS-CoV-2 was studied using molecular dynamics (MD) simulation. The RTP maintained the interactions observed in the experimental cryo-EM structure. Next, we designed new analogues of RTP, which not only binds to the RNA primer strand in a similar pose as that of RTP, but also binds more strongly than RTP does as predicted by MM-PBSA binding energy. This suggest that these analogues might be able to covalently link to the primer strand as RTP, but their 3' modification would terminate the primer strand growth.

Keywords: Remdesivir derivatives; RNA polymerization inhibitor; RdRp; Binding mechanism; Molecular Dynamics Simulations

INTRODUCTION

The world today faces difficult times with the current coronavirus pandemic. As of September 2021, there are almost 219 million people infected by the SARS-CoV-2 virus with approximately 4.55 million deaths spread in 220 countries around the globe. The lack of effective therapeutics and rapid transmission of the virus has exacerbated the course of infection, which left a huge burden on almost all aspects of human life. There is some hope with SARS-CoV-2 vaccine development, however, due to the fact that not every individual may develop neutralizing antibodies, as well as the possibility of side effects which may emerge in the future, the development of small molecule antiviral drugs is urgently needed.

SARS-CoV-2 has many viral proteins that can be targeted by small molecules. Among them, RNA-dependent RNA polymerase (RdRp) has become an attractive target, as it exists only in viruses and not in humans, and it exhibits active site conservation around coronavirus. Remdesivir, an analogue of adenosine triphosphate (ATP) which targets RdRp, was originally a drug developed for the treatment of Ebola virus[1, 2], but has recently undergone emergency clinical authorization for the treatment of Covid-19. Although it performed well in the previous in-vitro and in-vivo preclinical studies[3, 4], its clinical use in treating Covid-19 patients has been halted because it failed to show the significant improvement that was initially expected.[5-7] Therefore, the development of more potential analogues is an urgent research priority.

Studies have indicated that the active form of Remdesivir (Remdesivir triphospahate, RTP) works by delayed chain termination mechanism, in which the RTP halt RNA primer strand extension at the i+3 site after Remdesivir monophosphate (RMP) is incorporated into the RNA primer strand and translocated +3 steps, through stalling the further translocation of the primer strand [8, 9]. In that scheme, a nucleotide addition-inhibition cycle (NAC) consists of several

sequential states in term of the active site of the primer strand, i.e., an open active site conformation without NTP substrate binding (S1, PDB ID 6M71) [10], initial binding mode of NTP substrate (S2) to the active site of the primer strand, the conformational changes of the active site transition from an open state (S2) to a closed state accompanied by repositioning of the NTP (S3) and the key catalytic residues, the phosphoryl transfer reaction leading to a reaction product (S4, PDB ID 7BV2) [11], and finally i to i+3 translocation of the primer strand (S5) [12-14]. In a similar way, it was implied by some groups that the mechanism of a NTP substrate loading includes its adoption of the pre-insertion state and its binding to an open active center conformation and further folding of the trigger loop of the primer strand then leading to a closure of the active center, delivery of the NTP to the insertion site, and formation of all key contacts required for catalysis [15, 16]. More recently, Romero et al. (2021) studied the active-site open state of SARS-CoV-2 RdRp using apo form RdRp (PDB ID 7BTF) for the nucleotide initial binding and an closed active site of the polymerase using a reaction product (PDB ID 7BV2) for the stabilized nucleotide insertion, prior to catalytic addition of the nucleotide to the synthesizing primer RNA chain[17]. They implied that the initial binding and nucleotide insertion were guided by base stacking and base pairing with the template nucleotide, respectively [17]. In this study, we used the reaction product structure (PDB ID 7BV2) as a starting structure for building the initial complex structure of the non-covalent binding step of RTP and its analogues to SARS-CoV-2 RdRp and monitoring their conformational stabilities using molecular dynamics simulation (MDS). It is worth to mention that the reactant complex structure (i.e. Remdesivir in the closed-active state of RdRP) is not yet available. Only 2 SARS-CoV-2 RdRp structures complexed with Remdesivir available in Protein Data Bank at present, i.e., 7BV2 and 7L1F, which are the reaction product and delayed translocation structures of RdRp-Remdesivir complexes, respectively.

We previously obtained mechanistic binding insight of the active form of Remdesivir (RTP) to SARS-CoV-2 RdRp through homology modeling structure and the semiempirical method in deriving RTP ligand force field parameters.[18] Currently, we studied the system by using SARS-CoV-2 RdRp cryo-EM structure and the quantum mechanics method in deriving ligand force field parameters. The quantum mechanics method was selected due to its high accuracy in deriving force field parameters. The conformational change of the RdRp-RTP/protein-ligand system was monitored for 1 μs a using MDS. In addition, we designed new analogues (R1T, R2T and R3T) of RTP not only to cap the RNA polymerization, but also to enhance the binding affinity toward RdRp. Indeed, we discovered that our designed compounds exhibited a similar binding mode to RTP but with a much higher affinity.

MATERIALS AND METHODS

The RdRp complex structure was retrieved from the RCSB data bank with PDB ID 7BV2 [11], which was the closed active site conformation as indicated by the highly stabilized base pairing with template [17]. From this structure, it was necessary to only select the chain that had the catalytic site, so although the 7BV2 structure consists of multiple protein chains, only protein chain A plus two RNA chains (chains P and T) were selected. The protein-RNA complex was prepared using the Protein Preparation Wizard of Maestro software,[19] where it was pre-processed and optimized at pH=7 using default settings.

The RTP structure was downloaded from the PubChem database. In order to produce RTP-like compounds, we performed combinatorial synthesis using combinatorial library enumeration of the Maestro CombiGlide module.[20] Three compounds, i.e. R1T, R2T, and R3T, were selected based on RTP binding mode. The force field for RTP, R1T, R2T, and R3T molecules (**Figure S1**) were

developed in-house by generating charge models of nucleosides RN, R1N, R2N, and R3N (**Figure S2**) using the standard AMBER protocol,[21, 22] and merging them with the tri-phosphate force field developed by Carlson and coworkers (**Figure S1**).[23] In addition, 5'-form (R5), 3'-form (R3), and the middle-in-chain form (R) of Remdesivir nucleosides were created based on the AMBER protocol (**Figure S3)**. RNA OL3 and triphosphate parameters were assigned to each molecule and the GAFF force field was used to determine the remaining parameters (e.g. bond, bond angle, torsion, proper and improper dihedral angles).[23-25]

First, only the molecular electrostatic potential (MEP) of the nucleosides (**Figure S2**) were calculated at the HF/6-31G* methodology level using Gaussian 09. Then, geometry optimization was performed at the same level. MEP was then used to calculate the partial charges of all atoms in the nucleosides using the Restrained Electrostatic Potential (RESP) method with two-stage fitting and the use of multiple molecular orientations.[21] Partial charge constraints on each molecule is shown (**Figure S1-3**), which retains necessary solved partial charges of RNA nucleosides.[22] After successful RESP calculations, the finalized nucleosides were merged with the triphosphate parameters from PARM94 and ATP to construct RTP, R1T, R2T, and R3T (**Figure S1**). Geometry optimization, MEP, and RESP were not done on the RTP and its derivatives because an additional triphosphate group is too computationally-expensive and is thus why we opted to merge the triphosphate group and its parameters with each RNA nucleoside following the AMBER protocol.

Five systems in complex with the covalent form of R3 and non-covalent forms of RTP, R1T, R2T, and R3T were created for molecular dynamics simulation (MDS) (**Table S1**). While R3 was based on the solved crystal structure, RTP, R1T, R2T, and R3T were docked to *i* site (**Figure S15**) of crystal structure of RdRp employing Maestro's extra precision (XP) docking procedure with

the restraints to keep the R3 crystal conformation as much as possible. RTP pose is consistent with the pose of R3 (**Figure S16**), as for R1T, R2T, and R3T. Therefore, our dock pose is a good starting pose for sampling the reactant state of the complex structure. AMBER protein ff14SB[26] and RNA OL3[27, 28] force fields were used to represent protein and RNA, respectively. The protein-RNA net negative charges were neutralized by K+ ions. In addition, the salt was added to achieve 0.15 M KCl concentration.

AMBER16 was employed to perform Molecular Dynamics Simulation (MDS), following the protocol used in our previous studies.[29-37] Three independent runs of 1 μs for the RTP-RdRp system were performed to assess their conformational changes. Each system for R3, R1T, R2T, and R3T underwent MDS for 1 μs in addition to three independent runs of 200 ns for each R1T, R2T, and R3T; hence in total, 8.8 μs MDS were conducted for all systems. The run included a 1.0 ns MDS using the NPT ensemble mode (constant pressure and temperature) to equilibrate the system's density, following a 1000 ns dynamics in the equivalent NVT ensemble mode (constant volume and temperature). The SHAKE algorithm was used to treat all bonds interconnecting hydrogen atoms with a 2.0 fs time step in each simulation. The particle-mesh Ewald method[38] was used to treat long-range electrostatic interactions under periodic boundary conditions (charge grid spacing of ~1.0 Å, the fourth order of the B-spline charge interpolation; and direct sum tolerance of 10^{-5}). Short-range non-bonded interactions were defined at 10 Å and long-range interactions were treated with the uniform-density approximation. A two-stage RESPA approach[39] was used to calculate non-bonded forces. Short-range forces were updated every step, and long-range forces were updated every two steps. The Langevin thermostat was used to control temperature with a coupling constant of 2.0 ps. Trajectories were saved every 50.0 ps for analysis. The RMSD, RMSF, hydrogen bond, and clustering analysis were based on the combined

trajectories of MDS using CPPTRAJ module [40]. The clustering analysis was performed using DBSCAN [41], in which the RMSD was chosen as the distance metric with distance cutoff for forming a cluster (*epsilon*) and the minimum number of points/structures to form a cluster (*minpoints)* were 2.5 Å and 10, respectively, while other settings followed our previous protocol [18]. The H-bond analysis was conducted using default setting (Donor-Acceptor distance:3.5Å, and the Donor-Hydrogen-Acceptor angle >90 degree). We further calculated binding free energy of each system using the trajectory by employing MM-PBSA methods[42] and then predicted the ADME (Absorption, Distribution, Metabolism, Excretion) properties for RTP, R1T, R2T, and R3T by using the SwissADME web server (http://www.swissadme.ch).[43] Binding free energies were calculated using the python modules on 250 snapshots taken from 0 to 1 μs simulation trajectories as implemented in AMBER16. The polar contribution to solvation free energy was calculated by solving the Poisson-Boltzmann (PB) equation using a grid size of 0.5 Å, while the non-polar contribution was calculated using the solvent accessible surface area (SASA) with solvent-probe radius set to 1.4 Å.

Multiple Sequence alignment

To identify critical residues for catalysis of SARS-CoV2 RdRP, its primary sequence (uniprotein ID: QHD43415_NSP11) was used as a query to search its closest protein family (PF00680/Viral RdRP family) on the protein families database (pfam 33.1) (http://pfam.xfam.org/)[44]. Next, a multiple sequence alignment using MAFFT method [45] in Jalview [46] was performed to identify conserved residues in PF00680 plus SARS-COV2 RdRP (See **Figure S18**). Four critical Asp residues (D618, D623, D760 and D761) near the two Mg2+ ions in the product structure of RdRp (PDB 7BV2) were identified to be 100% conserved, likely playing a critical role in catalysis.

RESULTS AND DISCUSSION

Force Field Development for RTP, R1T, R2T and R3T and validation

Before developing the force fields for RTP, R1T, R2T and R3T, we took note of the structural similarities and differences that RTP and ATP share, which served as the basis for our strategy: Restrain the atom properties (atom name, type and partial charges) that RTP and ATP share, and change said atom properties where RTP and ATP differ. Fortunately, the AMBER RNA OL3 force field contains the full PARM94 parameters of ATP (**Figure S1A**) and its nucleosides A, A3, A5, and AN, in which the force fields of R, R3, R5 (**Figure S3**), RN, R1N, R2N, R3N (**Figure S2**), RTP, R1T, R2T, and R3T (**Figure S1B-E**) were derived.

Validation of the 7BV2 crystal structure with protein, RNA and R3 ligand covalently-bound to RNA is represented via a protein-RNA RMSD plot (**Figure S13**) and a structure comparison figure between the reference and last snapshot structure complexes 7BV2 from a 1 μs MD simulation (**Figure S14**); to note, since R3 is covalently-bound to RNA, it is incorporated in the RNA RMSD. The simulation system reached convergence quite early at ~200 ns and maintained an RMSD value of ~ 2 Å for the remainder of the simulation (**Figure S13**). This implies that the overall structure conformation of 7BV2 changed negligibly, which we show in the next figure (**Figure S14**). Between the reference and last snapshot structure complexes, the protein, RNA and R3 ligand show significant overlap with one other. Our simulation thus validates the stability of the crystal structure complex.

RTP binding to RdRp complex

The SARS-CoV-2 RdRp structure contains 11 bases in the primer strand, 14 bases in the template strand, and two Magnesium ions. RTP was docked at the *i* position of the RdRp catalytic site,

where *i* is the location where RTP is incorporated. The docking pose of RTP was similar to the crystal 7BV2 covalently bound R3, in which the phosphate group was positioned at the entry of the NTP channel formed by hydrophilic residues (K545, R553, and R555)[10], which would inhibit the entry of NTP to the RdRp active site. In addition, the reactant state of SARS-CoV-2 RdRp was indicated by the coordination of two Magnesium ions with RTP, D618, D623, D760, and D761 of RdRp active site [47, 48]. **Figure 1** shows the 3D conformation of RTP in the RdRp SARS-CoV-2, the detailed interaction of docked RTP with RdRp, and the RTP interactions with two Magnesium ions, D618, D623, D760, and D761 of RdRp active site, while **Figure S16** depicts the superimposed comparison of crystal 7BV2 covalently bound R3 to docked RTP. Our multiple sequence alignment of SARS-COV2 RdRP to its protein family (PF00680) suggest these ASP residues (D618, D623, D760 and D761)) are 100% conserved in the family (**Figure S18**), thus likely being key catalytic residues for the catalysis [49].

A

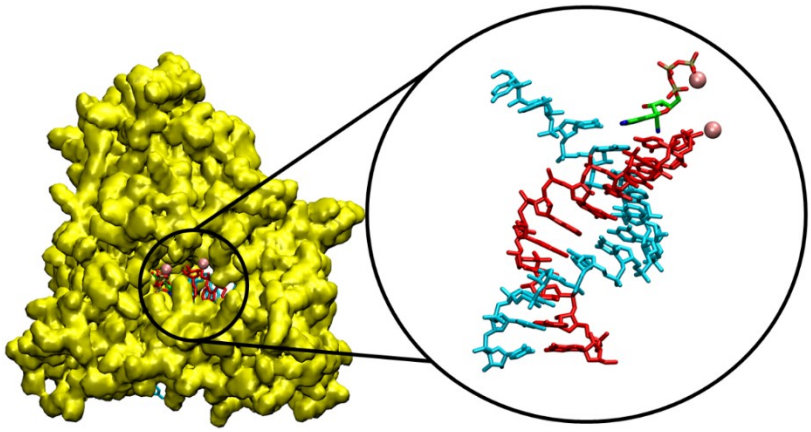

B

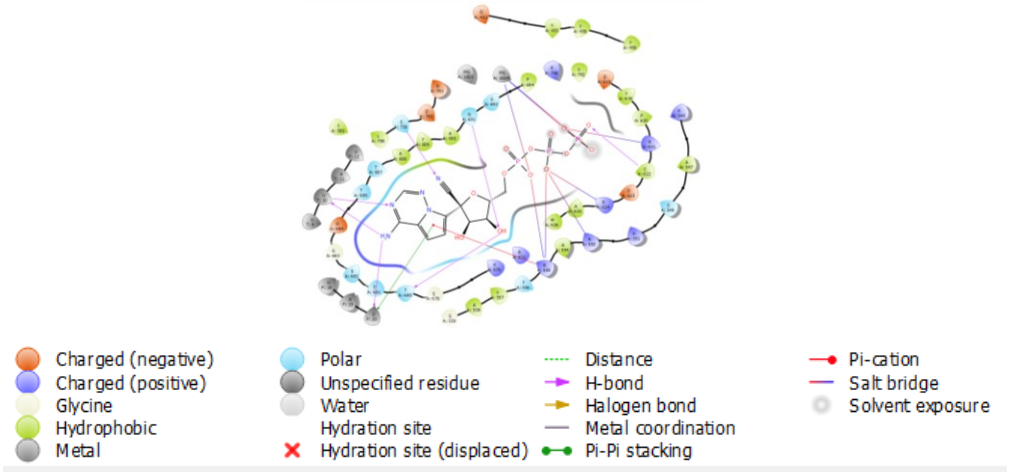
Charged (negative)
Charged (positive)
Glycine
Hydrophobic
Metal
Polar
Unspecified residue
Water
Hydration site
Hydration site (displaced)
Distance
H-bond
Halogen bond
Metal coordination
Pi-Pi stacking
Pi-cation
Salt bridge
Solvent exposure

C

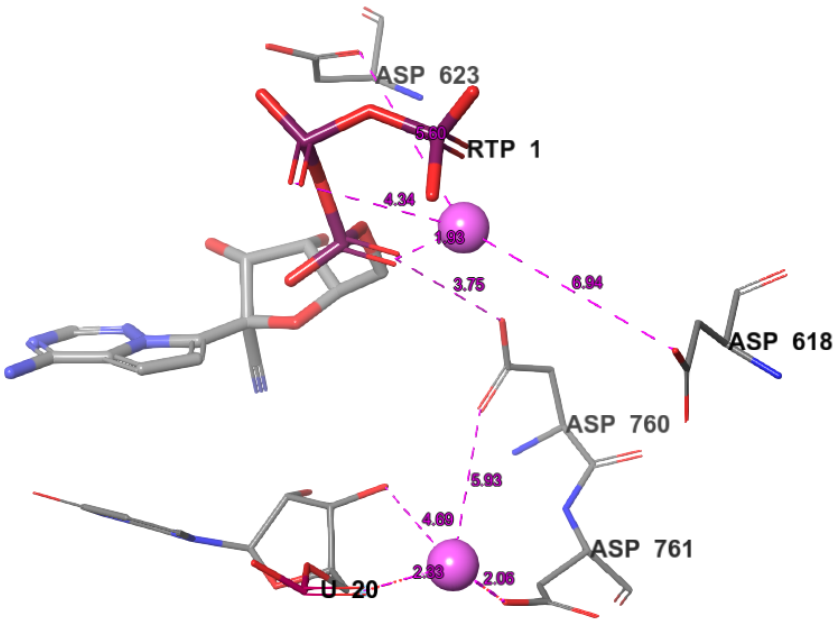
ASP 623
RTP 1
5.00
4.34
1.93
3.75
6.94
ASP 618
ASP 760
5.93
4.69
ASP 761
U 20
2.83
2.06

Figure 1. The 3D surface representation of RdRp and conformation of RTP in the RdRp SARS-CoV-2 (**A**) and the detailed interaction of docked RTP with RdRp (**B**). Template and primer RNA strands are colored in cyan and red, respectively. The RTP interactions with two Magnesium ions (colored in pink), D618, D623, D760, and D761 of RdRp active site, in which distance was measured in Angstrom (**C**).

Gong and Peersen (2010) proposed the sequential catalytic cycle model of poliovirus polymerization [50], in which **state 1** is an apo form of initial structure without a bound NTP (PDB code: 3OL6, which is comparable with 6M71 for SARS-CoV-2). **State 2** is an open active site with NTP non-covalently bound without Mg ions (PDB code: 3OLB). **State 3** is closed active site conformation with NTP non-covalently bound and presence of Mg ions. Of note, the crystal structure of **State 2** and **State 3** is not yet available for SARS-CoV-2. **Table S2** depicts the comparison of RdRp structures of poliovirus, Norwalk virus, and SARS-CoV-2 virus in each state recorded in Protein Data Base (PDB).

Zamyatkin et al (2007) proposed the crystal structure of **State 3** of Norwalk virus (PDB ID: 3BSO), in which MnA ion was coordinated with D671 (D343) (distance 2.15 Å) and Pα (2.18 Å), while MnB ion was coordinated with D570 (D242) (distance 2.15 Å), Pα (distance 2.41 Å), Pβ (distance 2.08 Å) and Pγ (distance 2.16 Å) groups (**Figure S19B**) [51]. In our reactant state, the distances become longer, in which those between MgA and D760 and between MgB and D618 were 5.93 Å and 6.94 Å, respectively (**Figure 1C**). We showed the superimposition of the **State S3** of Norwalk virus (PDB ID: 3BSO) and the reaction product (**State 4**) of SARS-CoV-2 (PDB code: 7BV2) in **Figure S19A** and **Figure S19D**.

State 4 is a closed active site of post catalysis pre-translocation with NTP bound covalently and presence of Mg2+ ions (PDB code for poliovirus: 3OL7, comparable with 7BV2 structure in SARS-CoV-2), the superimposition of 7BV2 and 3OL7 was depicted in **Figure S20A** and **Figure S20C**. As can been seen from **Figure S20B**, the distances between MgA ion and D328 and between

MgB ion and D233 of poliovirus were 2.86 Å and 3.06 Å, respectively, both ions were coordinated with phosphate groups. However, the distances become longer in the SARS-CoV-2 virus, in which those between MgA ion and D760 and between MgB ion and D618 were 6.25 Å and 6.41 Å, respectively (**Figure S19C**). Thus, the longer distances between metal ions and key residues observed in our current study (**Figure 1C**), is consistent with the longer distances revealed in the experimental structure of reaction product (**State S4**) of SARS-CoV-2 (PDB ID: 7BV2). It is clear that while MgB ion positions are conserved in Norwalk, poliovirus, and SARS-CoV-2 viruses, the MgA ion of SARS-CoV-2 is located at more upstream site than those found in Norwalk (differing by 3.37 Å) and poliovirus (differing by 2.99 Å) (**Figure S19D and S20C**). It is likely due to the protein sequence change from poliovirus and Norwalk virus to SAR-CoV-2 and is a hallmark for the latter. However, further experimental study is needed to clarify the issue.

Adenosine groups of RTP formed H-bond interactions with U10 of the template strand and U20 of the primer strand. Additionally, Pi-Pi orbital stacking interactions were formed between the adenosine motif and U20 of primer strand, which was also observed in the experimental structure.[11, 52] The ribose ring 3'-OH atom formed H-bond interactions with N691 and T680 in RTP, while the cyano group formed H-bond interactions with S759. The phosphate group of RTP formed salt bridge interactions with positively charged amino acid residues K621, R555, and R624. The triphosphate group of the ligand was additionally stabilized by Mg^{2+} ions through metal coordination and salt bridge interactions as found in the experimental structure.[11] In the RTP complex, D623 and D760 were located close to triphosphate and magnesium ions. In brief, our docking pose is consistent with the experimental structures of RTP and RdRp complexes.

During the 1 μs MDS, several H-bond interactions were retained. The RTP H-bond interactions occurring with K621 (K252) and U10 (U542) of the template strand were preserved at high

occupancies (79.6% and 64%, respectively), while the H-bond with R555 (R186) was maintained at modest occupancy (57.6%). **Table S2** showed the H-bond occupancies of RTP during 1 μs MDS. Clearly, the RTP was able to maintain H-bond interactions with active site residues of RdRp.

The trajectory convergence during MDS was checked through the RMSD values averaged over three independent 1 μs MDS for protein Cα, RNA, and ligand heavy atoms for RTP complex (**Figure S19**). The receptor Cα achieved stability around 100 ns and remained stable towards the end of simulation time. The RMSD of RNA main atoms shows more fluctuation at around 2 Å and remains stable during MDS. The ligand RMSD of RTP did not change significantly during the simulation time. Fluctuations of RMSD values of ligand-heavy atoms were around 1 Å. The RMSD values of the RTP system were shown to be nearly constant during 1 μs MDS, which implied that the RTP attained a stable conformation in the RdRp active site. The RMSD values for the first, second, and third MDS of RTP show similar patterns (**Figure S20**).

The fluctuation of protein amino acid residues during MDS was shown in the RMSF plot (**Figure S21**). The high peaks of residues were observed at V405, G432, T644, and G823, which corresponded to the protein loops, while E370 and L895 were the protein carboxy and amino ends. The residues R555, K621, D623, R624, T680, N691, S759, and D760, which directly interacted with RTP, were found to be stable.

The fluctuation of RNA O5' and ligand heavy atoms was depicted in **Figure 2**. The RMSF values of RNA O5' atoms of the RTP system were observed to be stable under 3 Å. High peaks were observed in G10, which is the primer strand end, as well as U8 and C21, which are the template strand ends. The U10 and A11 of template strands, which are observed to form the H-bond interactions with RTP, were observed to be stable, while the RMSF values of RTP heavy atoms were observed to be stable under 1 Å, which confirmed the RMSD values of ligands.

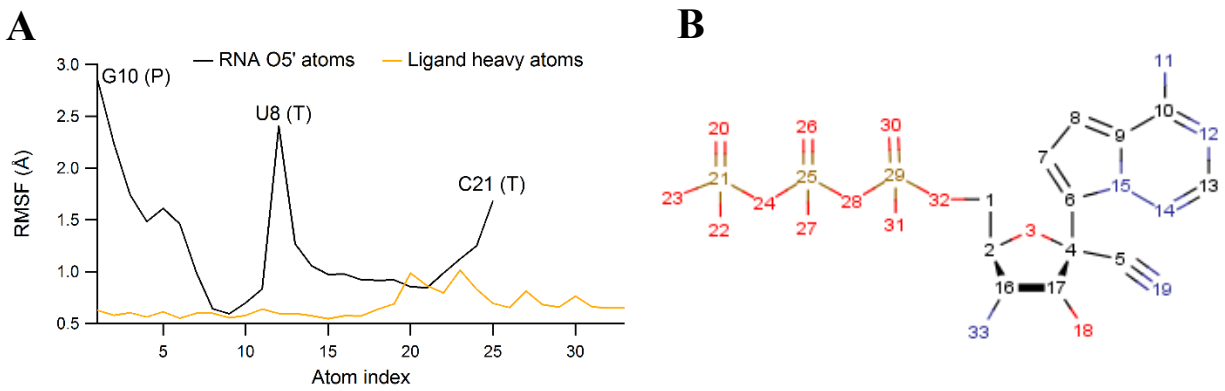

Figure 2. The RMSF plot of RNA O5' atoms (black) and ligand heavy atoms (orange) (**A**) and labeled 2D structure of RTP (**B**).

Clustering analysis of RTP complex

Figure 3A shows the representative structure of the most abundant cluster from the cluster analysis extracted from MDS trajectories, in which there was only one cluster with 100% population. The RTP interactions with two Magnesium ions, D618 (D249), D623 (D254), D760 (D391), and D761 (D392) of RdRp active site were depicted (**Figure 3B**). It was shown that RTP confirms the H-bond interactions with S759 through O4' of the ribose ring, and with R555 through the triphosphate group while maintaining close distance with D618, D760, and D761. In addition, a 3' hydroxyl group of ribose rings formed H-bond interactions with D623, which was also found in the previous experimental study.[53] Researchers Yin et al (2020) indicated that the S759, D760, and D761 residues comprise the catalytic active center of RdRp[11], while Gao et al., (2020) indicated that R555, V557, and D618 were among the key binding residues.[54] Moreover, magnesium ions were located near the triphosphate group of RTP, and aspartate residues which indicated their role in stabilizing ligand conformation as indicated in the experimental structure.[11] Prior studies have shown that incorporation of RTP at position *i* will block viral RNA synthesis through delayed chain termination mechanism at positions *i*+3 or *i*+5, which is responsible for antiviral activity of Remdesivir[53, 55, 56], as per present results.

A

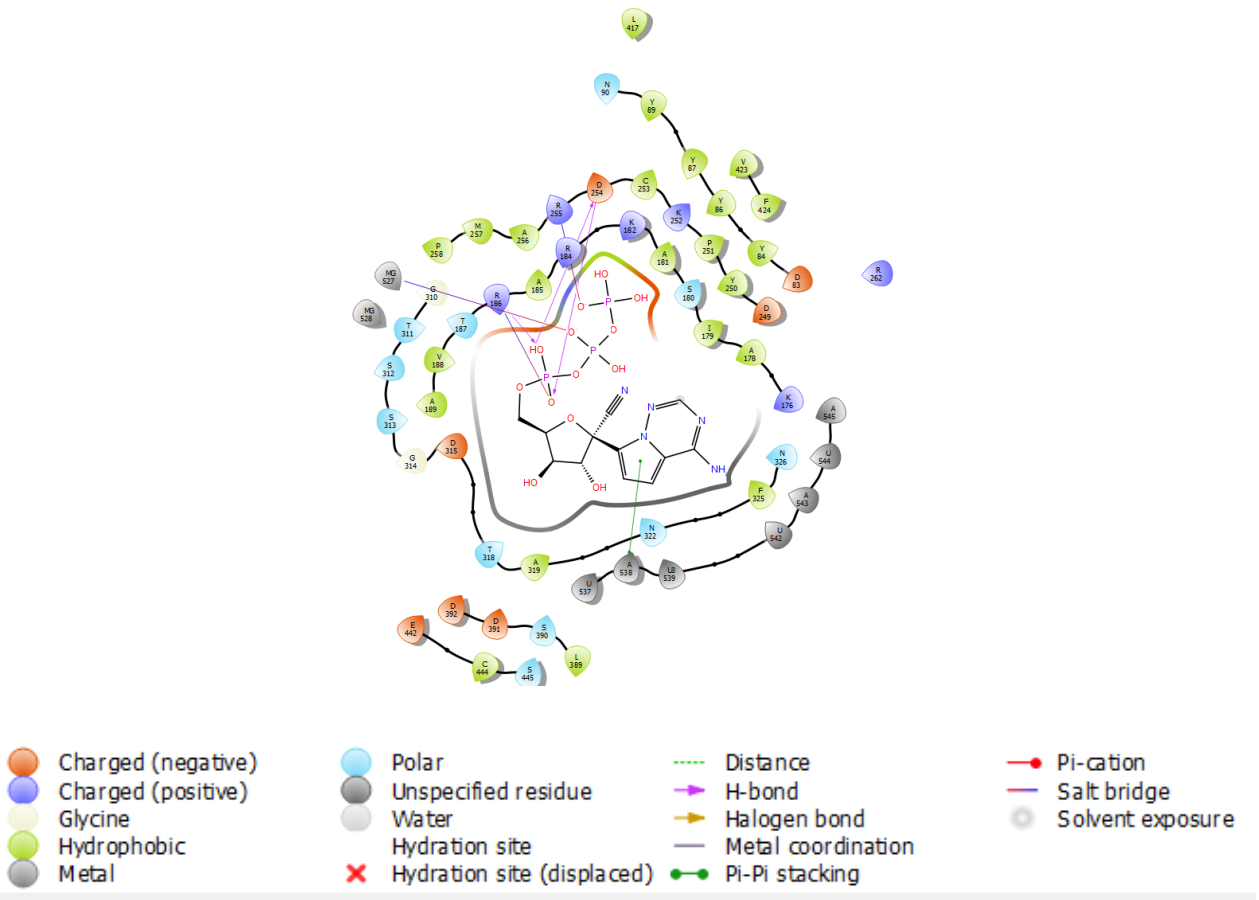

B

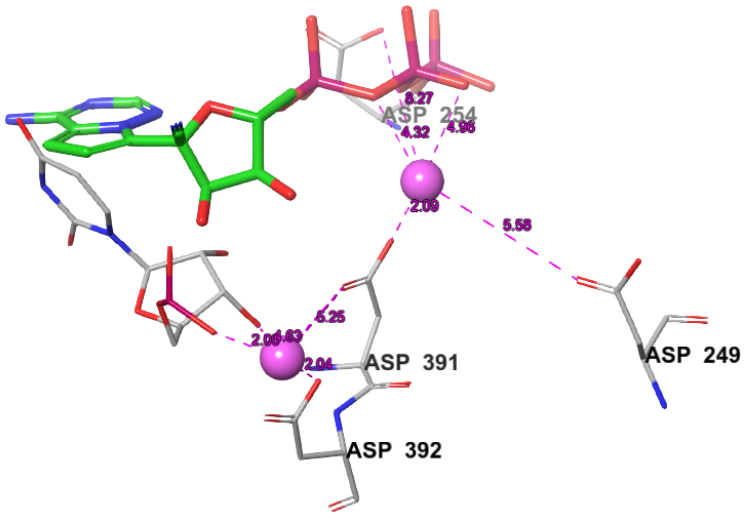

Figure 3. The detailed interaction of the most dominant cluster of RTP with RdRp (A). The RTP interactions with two Magnesium ions (colored in pink), D618 (D249), D623 (D254), D760 (D391), and D761 (D392) of RdRp active site, in which distance was measured in Angstrom (**B**).

Designing New Analogues

To improve the binding affinity of RTP, we performed combinatorial library enumeration which resulted in three RTP analogues, i.e. R1T, R2T, and R3T. The structures of RTP analogues were varied in ribose 3'OH group as shown in **Figure 4**.

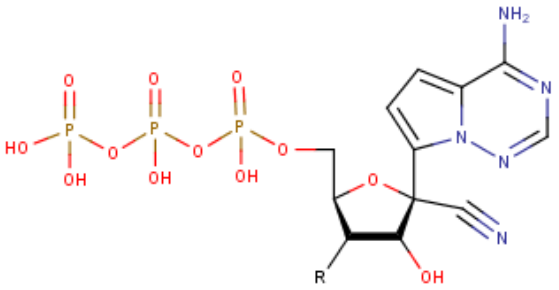

Ligand	R-Substituent
RTP	OH
R1T	H
R2T	NH_2
R3T	$NHCH_3$

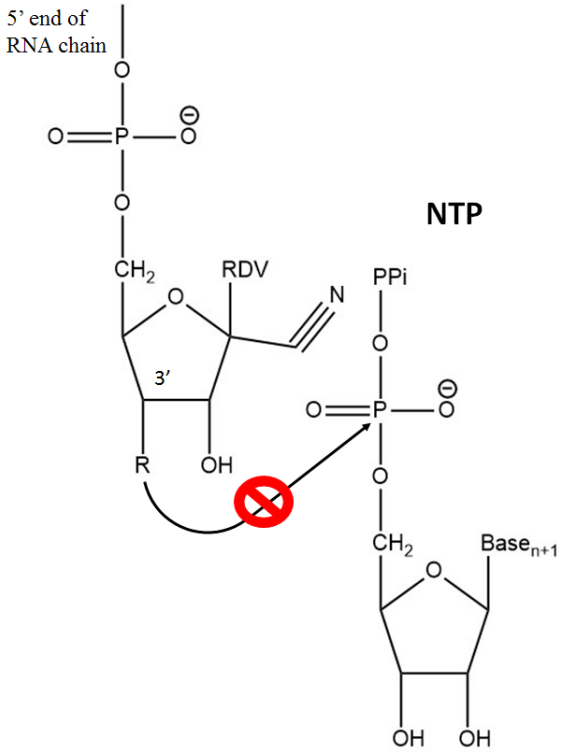

Figure 4. The structures of designed RTP analogues (left) and schematic diagram showing the inhibition of 3'OH atom attack to the α-phosphate of NTP (right).

The docking conformations of R1T, R2T, and R3T were essentially similar to the RTP pose. The H-bond and base stacking interactions were observed between the adenosine parts, template strand, and primer strands, respectively. The ribose ring hydroxyl group formed H-bond

interactions with N691 in R1T, R2T, and R3T, while the phosphate groups interacted with positively charged amino acid residues K621 and R555. The aspartate residues and magnesium ions were observed to be close to phosphate groups of ligands. **Figure 5** depicts the 3D surface representation of RdRp and conformation of R1T, R2T, and R3T analogues in the SARS-CoV-2 RdRp.

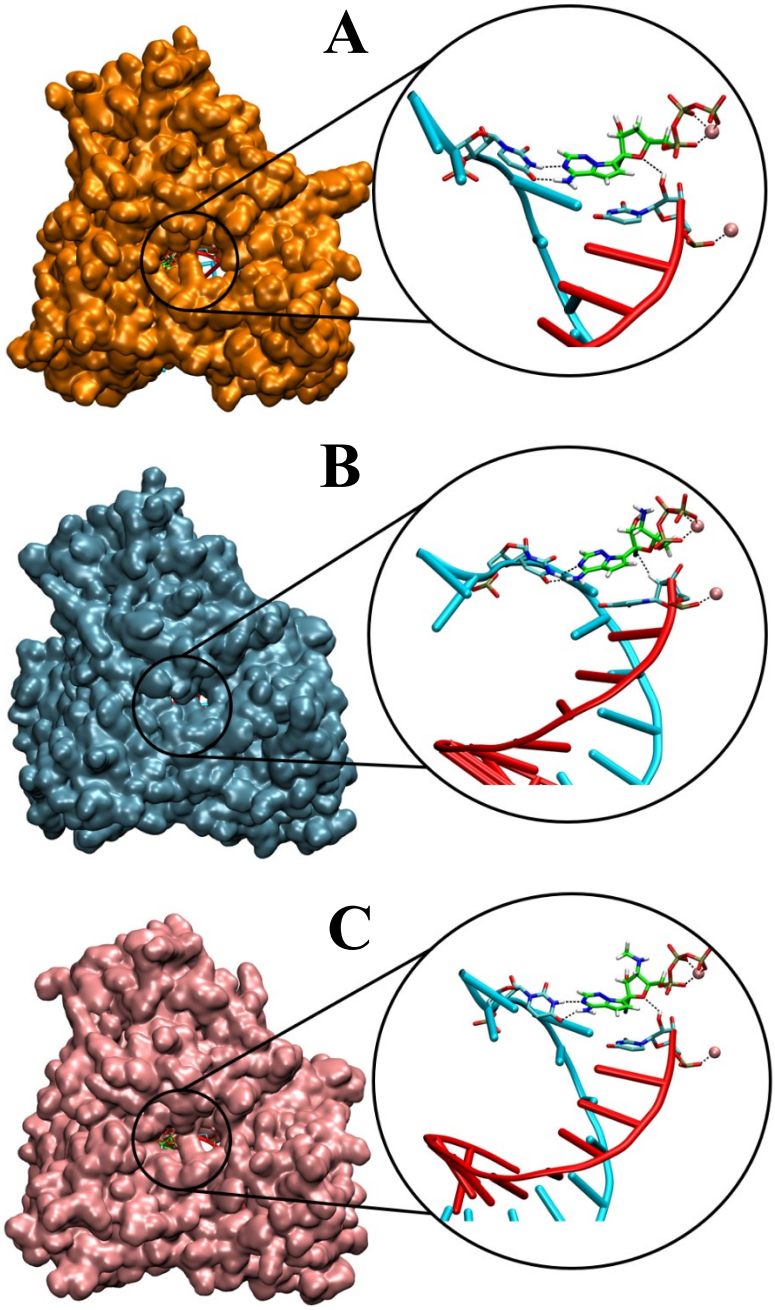

Figure 5. The 3D surface representation of RdRp and conformation of R1T (**A**), R2T (**B**), and R3T (**C**) analogues in the SARS-CoV-2 RdRp. Template and primer RNA strands are colored in cyan and red, respectively. Magnesium ions are colored in pink.

We then conducted three independent runs of 200 ns for each R1T, R2T, and R3T to evaluate the complex stabilities and their binding affinities. We found out that the RTP analogues were all very stable during 3x 200 ns (**Figure S25-S28**) and their binding affinities was also lower than that of RTP complex (**Table S6**). Further we performed individual MDS for 1 μs for each compound, i.e. R1T, R2T, and R3T. **Figure S35** shows the RMSD values for protein Cα, RNA and ligand heavy atoms for 1 μs. The protein Cα RMSD values for R1T and RTP were nearly identical, while those for R2T and R3T were shown to be higher and lower than RTP, respectively. However, these two are stable enough despite fluctuation under 3 Å complexes. Some fluctuation was recorded in RMSD values of R3T RNA heavy atoms, while those for R1T and R2T were comparable to RTP. The RMSD values of ligand heavy atoms are quite stable in all complexes.

The protein RMSF profiles show that R2T generally enhances more flexibility in protein compared to RTP, which is consistent with the RMSD plot of protein Cα, as well as showing similar patterns between complexes. Fluctuation occurred at S384, T402, T644, and D824, which were protein loops (**Figure S36**). Other residues were noticed to be stable.

The RMSF values of RNA O5' and ligand heavy atoms are shown in **Figure 6**. The RNA RMSF pattern of R1T, R2T, and R3T were very similar to the RTP. High atomic fluctuations were recorded in G10 (primer strand end), U8, and C21 (template strands ends), while U10 and A11 of the template strands were observed to be stable, as found in the RTP complex. The RMSF values of ligand main atoms were observed to be stable under 1.6 Å. The highest peak was observed in

O2’ atoms of the ribose hydroxyl group of R3T. However, its fluctuation was considered to be stable.

A

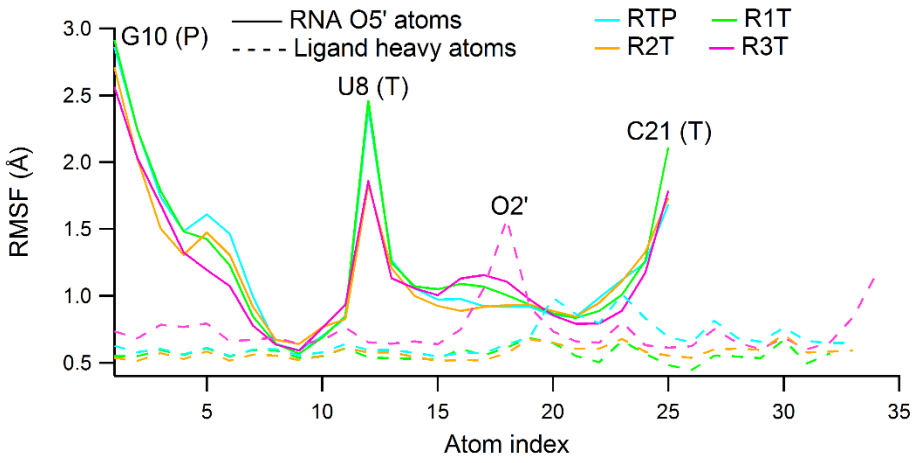

B

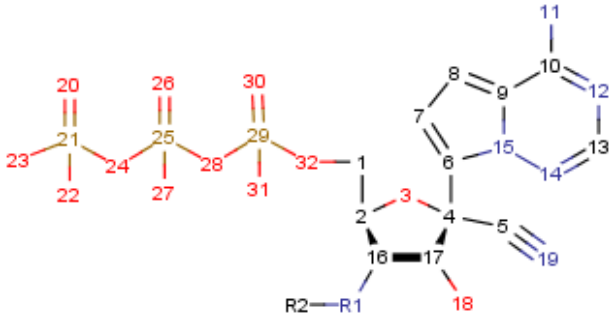

Ligand	Atom number	
	R1	R2
RTP	33	N/A
R1T	N/A	N/A
R2T	33	N/A
R3T	33	34

Figure 6. The RMSF values for RNA O5’ and ligand heavy atoms for RTP (blue), R1T (green), R2T (orange), and R3T (purple) (**A**). Labeled 2D structure of R1T, R2T, and R3T (**B**).

Clustering analysis of analogues complexes

In the cluster analysis of analogues complexes, each compound, i.e. R1T, R2T, and R3T, was able to reproduce the H-bond interactions between amino groups of adenosine part and U10 (U542) of template strands. The R1T, R2T, and R3T compounds were also able to reproduce H-bond interactions between phosphate groups and R555 (R186) (64.8%, 70.9%, 85.4%,

respectively, for R1T, R2T, and R3T) and K621 (K252) (79.3%, 72.1%, 82.5%, respectively, for R1T, R2T, and R3T) (**Table S3-S5**) as well as pi-stacking interactions between adenosine motif and A11 (A543) of the template strand. All of those interactions were observed in RTP conformation.

The presence of amino groups in R2T and R3T would hypothetically block the nucleophilic attack on the α-phosphate of an incoming nucleotide as observed in RTP [53, 56]. As a result, we speculate that further nucleotide incorporation is still allowed which would lead to a delayed RNA synthesis inhibition.[57] In the case of R1T, further nucleotide addition would be prevented due to the absence of a ribose 3'OH group, and would eventually lead to classic chain termination.[57, 58] **Figure 4** presents the schematic diagram showing the inhibition of a nucleophilic attack of the 3'OH group on the α-phosphate atom of NTP, while **Figure 7A-C** shows the detailed interaction of the most dominant clusters of R1T, R2T, and R3T with RdRp.

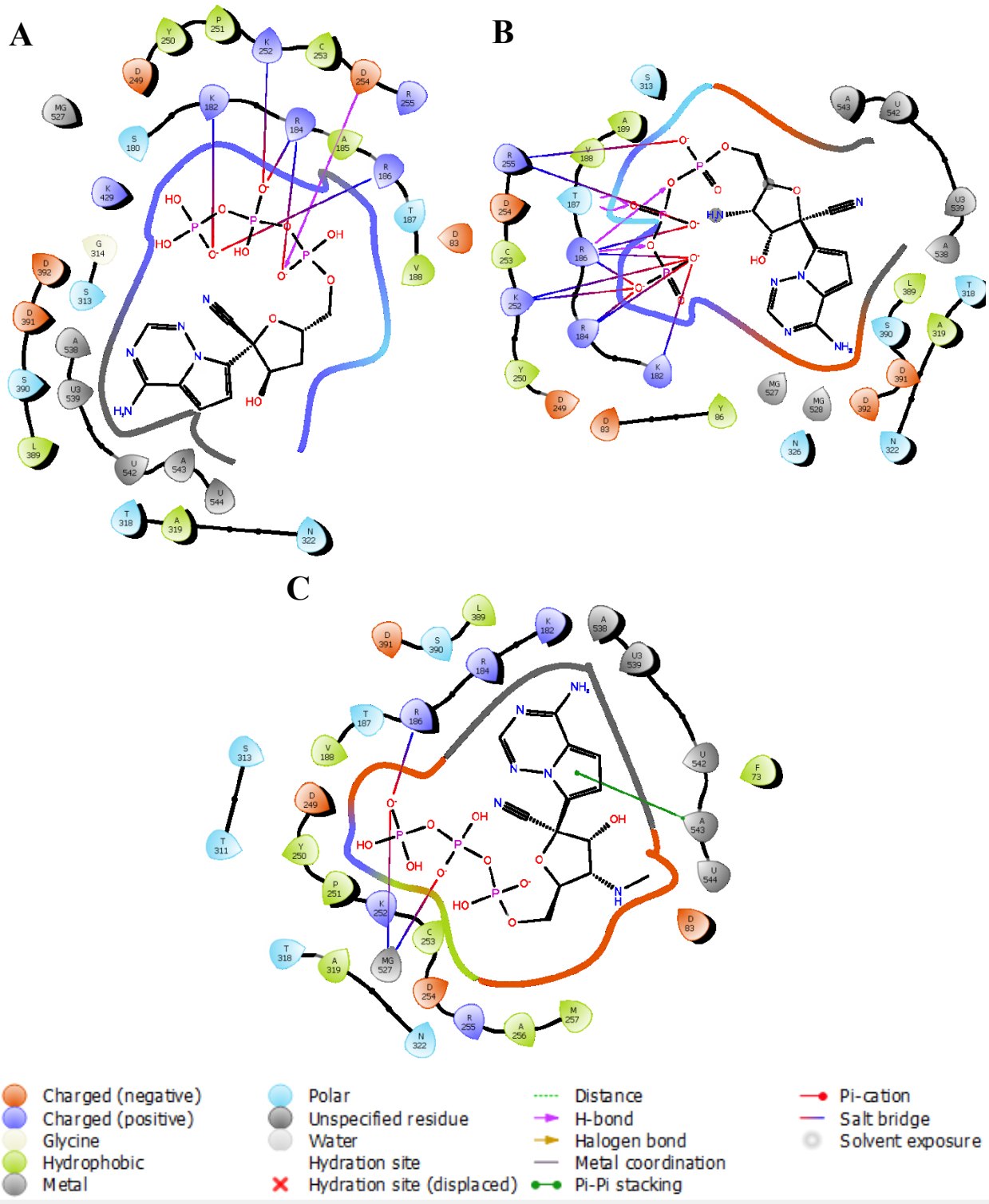

Figure 7. The detailed interaction of the most dominant cluster of R1T (**A**), R2T (**B**), and R3T (**C**), each with RdRp.

Another interesting finding was that base pairing between RTP and U10 of template strand were maintained in 64% and 42.2% occupancies (**Table S2**), while those were 75.1% and 70.4% occurrences in R1T (**Table S3**), 70% and 47.6% occupancies in R2T (**Table S4**), and 78.6% and 45% occurrences in R3T (**Table S5**). It was clear that the RTP analogues maintain hbond base pairing better compared to RTP. In all ligand poses, D760 (D391) and Mg^{2+} ions were observed in close proximity to phosphate groups, indicating their important roles in ligand stabilization.[59] Clearly, the R1T, R2T, and R3T were able to reproduce the RTP interactions, while establishing more interactions with residues in the RdRp active site. Being that they have the ability to reproduce the RTP interactions, R2T and R3T are very likely to work in the same fashion as RTP in terms of inhibiting RNA polymerase specifically through chain delayed termination, while R1T would work through classic chain termination mechanism.[60]

Next, using 1 μs MDS trajectory, each ligand was investigated for their thermodynamic properties which is useful to obtain a deeper insight into the ligand and RdRp interactions. Here we used the MM-PBSA method to determine free energy of binding. **Table 1** shows the free energy of binding predicted by MM-PBSA protocol using 1 μs trajectory. As shown in **Table 1**, the electrostatic energies (ΔE_{ELE}) were favorable for binding in each ligand, and although the polar contribution for solvation (ΔE_{PB}) is unfavorable, the total electrostatic energy terms were still favorable. This is different from our previous work, which used a semi-empirical method to derive force field parameters, in which the total electrostatic contribution was unfavorable for RTP.[18] The present result is more reasonable in terms of the persistence of electrostatic interactions of nucleotides in the RdRp active site originating from interactions between the negatively charged ligand and positively charged residues, which was also previously reported.[61] This finding highlights the benefits of the quantum mechanics method over the semiempirical method in

describing protein-ligand interaction.[62] Furthermore, other favorable contributions originated from van der Waals (ΔE_{VDW}) and non-polar contribution for solvation (ΔE_{PBSUR}).

Table 1. The binding energies and their standard deviations predicted by MM-PBSA protocol calculated at 1 μs trajectory*

Ligand	ΔE_{ELE}	ΔE_{VDW}	ΔE_{PB}	ΔE_{PBSUR}	ΔE_{PBTOT}	$\Delta\Delta E_{PBTOT}$
RTP	−121.87±26.07	−29.31±7.46	87.19±21.17	−4.30±0.12	−68.24±6.40	0.00
R1T	−163.37±19.68	−31.40±6.38	114.08±14.16	−4.35±0.10	−85.04±6.21	16.80±6.21
R2T	−162.95±12.50	−29.49±6.85	111.73±8.14	−4.33±0.12	−85.04±7.14	16.80±7.14
R3T	−164.86±14.51	−36.69±6.30	115.36±10.52	−4.65±0.08	−90.85±6.98	22.61±6.98

*All values are in kcal/mol. $\Delta\Delta E_{PBTOT}$ is the relative binding energy with reference to the RTP.

It is worth noting that the R1T, R2T, and R3T showed higher affinities (−85.04 kcal/mol, −85.04 kcal/mol, −90.85 kcal/mol, respectively) toward RdRp as compared to RTP (−68.24 kcal/mol). The R1T, R2T, and R3T each enhanced the binding energy by 16.80 kcal/mol, 16.80 kcal/mol, and 22.61 kcal/mol, respectively. The more negative electrostatic contribution (ΔE_{ELE}) of R1T, the clearer it becomes that R2T and R3T contributed to their higher affinities. Additionally, the van der Waals energy (ΔE_{VDW}) of R3T is slightly more negative than that of R1T, R2T, and RTP, which explains its superior binding among other nucleotides. The data indicated that the replacement of the 3' hydroxyl group of the ribose ring with the alkyl amino group would enhance the nucleotide binding toward RdRp. As explained in the previous section, the alkyl amino which replaces the ribose 3' hydroxyl group could function as a nucleophile to attack the α-phosphate of the incoming nucleotide and release a pyrophosphate molecule with the help of magnesium ion and aspartate residues around the triphosphate group.[63, 64] In the present study, the entropy term

was not calculated due to complexity and that the entropy term can be neglected since all entropic contributions will be similar for very similar molecules [65, 66]. In brief, the present study proposes new molecules as potential candidates of RdRp inhibitors, which need in-vitro and in-vivo verification before their clinical use.

Prediction of ADME properties

Table S7 shows the predicted ADME properties for RTP, R1T, R2T, and R3T, while the complete list of ADME properties is shown in **Figure S37A-D**. All compounds show low intestinal absorption properties with no chance for distribution into the brain. They could not be inhibitors for the subtypes of cytochrome P450 enzymes (CYPs) including CYP1A2, CYP2C19, CYP2C9, CYP2D6, and CYP3A4, which indicated that they most likely could not be metabolized. They also share the same violation of Lipinski's rule of five, including molecular weight ((MW) > 500) and the number of H-bond acceptors ((NorO) > 10). Hence, all of the three designed analogues share the same ADME properties as RTP, which indicates their favorable use in prodrug form.

CONCLUSIONS

We developed the AMBER compatible ligand force fields of RTP, R1T, R2T, R3T, and three covalent forms (R5, R, and R3) of RTP by generating the partial charges for the corresponding nucleosides following the standard AMBER protocol, and merging them with the existing tri-phosphate force field and the remaining parameters from the AMBER force fields. Validation of our R3 force field was carried out by using the crystal structure R3-RdRP (PDB ID 7VB2). The experimental structure was well maintained so that our force fields are well enough to be used with AMBER protein and nucleic acid force field. With these ligand force fields, we studied the active

form of Remdesivir binding to SARS-CoV-2 RdRp using molecular dynamics simulations. We determined that RTP reproduced experimental structure interactions when binding to RdRp. We identified key residues for RTP binding, i.e. S759 and R555 through the triphosphate group, while maintaining close distance with D618, D760, and D761. Using the RTP binding mode, we designed new RTP analogues, R1T, R2T, and R3T, to enhance the binding affinity. Based on MM-PBSA binding energy calculations, it was shown that all of the RTP analogues R1T, R2T, and R3T bind more strongly to the RdRp active site as compared to RTP. The detailed interaction of all analogues showed that they were able to maintain base pairing through the adenosine part as well as maintain ionic interactions through the triphosphate group. Moreover, the designed analogues exhibited additional interactions through the amino and methyl amino groups of ribose ring in R2T and R3T, respectively. The MM-PBSA analysis showed that electrostatic contribution is the dominant factor in enhancing binding affinity. These findings allude to our hypothesis that the analogues would potentially be better RdRp inhibitors than RTP, however further study on the inhibition mechanism of those RTP analogues are necessary.

ASSOCIATED CONTENT

Supporting Information

Table S1 to S8 (Molecular dynamics simulation runs, The comparison of RdRp structures of poliovirus, Norwalk virus, and SARS-CoV-2 virus in Protein Data Base (PDB), Hydrogen bond occupancy between RTP and RdRp complex retrieved from 1 μs MD simulation, Hydrogen bond occupancy between R1T and RdRp complex retrieved from 1 μs MD simulation, Hydrogen bond occupancy between R2T and RdRp complex retrieved from 1 μs MD simulation, Hydrogen bond occupancy between R3T and RdRp complex retrieved from 1 μs MD simulation, The binding energies and their standard deviations predicted by MM-PBSA protocol calculated at 200 ns trajectory for R1T, R2T, and R3T, and at 1 μs trajectory for RTP, The ADME properties as predicted by the SwissADME web server), Figure S1 to S39 (Partial charge models of the adenosine triphosphate (ATP), RTP molecule and its derivatives, Partial charge model of neutral Remdesivir nucleosides, Partial charge model of Remdesivir nucleosides, MOL2 file of RTP molecule, MOL2 file of R1T molecule, MOL2 file of R2T molecule, MOL2 file of R3T molecule, MOL2 file of RN molecule, MOL2 file of R molecule, MOL2 file of R3 molecule, MOL2 file of R5 molecule, FRCMOD file for R, R3, R5, RN, RTP, R1T, R2T and R3T molecules, Validation plot for MD simulation of crystal 7BV2 with R3 ligand covalently-bound to RNA, Last snapshot structure complex of crystal 7BV2 with R3 ligand covalently-bound to RNA superimposed on its reference complex structure over a 1 μs MD simulation, The schematic diagram showing the *i* site, in which RTP and its analogues were docked, Superimposed comparison of crystal 7BV2 covalently bound RDV to docked RDV-TP, The reaction state (A), transition state (B), and reaction product (C) of 7BV2, Multiple sequence alignment of SARS-COV2 RdRp with its protein family (PF00680) and Human poliovirus 1 (3OLB_f), The superimposition of **State 4** of SARS-

CoV-2 (PDB code: 7BV2) and the **State S3** of Norwalk virus (PDB ID: 3BSO), The interactions between Mn2+ ions with key residues in **State S3** of Norwalk virus (PDB ID: 3BSO), The interactions between Mg2+ ions with key residues in **State S4** of SARS-CoV-2 virus (PDB ID: 7BV2), the superimposition of interactions between ions and key residues in **State S3** of Norwalk virus with those in **State S4** of SARS-CoV-2 virus, The superimposition of **State 4** of SARS-CoV-2 (PDB code: 7BV2) and the those of **State S4** of poliovirus (PDB ID: 3OL7), The interactions between Mg2+ ions with key residues in **State S4** of poliovirus (PDB ID: 3OL7), The superimposition of interactions between ions and key residues in **State S4** of poliovirus (PDB ID: 3OL7) with those in **State S4** of SARS-CoV-2 virus (PDB ID: 7BV2), The RMSD values for the receptor Cα, RNA and ligand heavy atoms averaged over three 1 μs runs for the RTP system, The RMSD values for the protein Cα, RNA and ligand heavy atoms of RTP complex tabulated from the first, second, and third trajectories, The RMSF plot of protein of RTP complex, Plot of protein RMSF of RTP complex tabulated from the first, second and third MD trajectories, The RMSF plot of RNA O5' atoms of RTP complex tabulated from the first, second, and third trajectories, The RMSF plot of ligand heavy atoms of the RTP complex tabulated from first, second, and third trajectories, The RMSD values for the protein Cα, RNA and ligand main atoms of R1T, R2T, R3T complexes, averaged from the first, second, and third trajectories, The RMSD values for the protein Cα, RNA and ligand main atoms of R1T, R2T, R3T complexes, tabulated from the first trajectory, The RMSD values for the protein Cα, RNA and ligand main atoms of R1T, R2T, R3T complexes, tabulated from the second trajectory, The RMSD values for the protein Cα, RNA and ligand main atoms of R1T, R2T, R3T complexes, tabulated from the third trajectory, Plot of protein RMSF of R1T, R2T, and R3T complex averaged from the first, second and third trajectories, Plot of protein RMSF of R1T, R2T, and R3T complex tabulated from the first, second and third MD

trajectories, The RMSF plot of RNA O5' atoms of R1T, R2T, and R3T complexes averaged from the first, second and third trajectories, The RMSF plot of RNA O5' atoms of R1T, R2T, and R3T complexes tabulated from the first, second and third trajectories, The RMSF plot of ligand heavy atoms of R1T, R2T, and R3T complexes tabulated from first, second and third trajectories, The RMSF plot of ligand heavy atoms of R1T, R2T, and R3T complexes tabulated from first, second and third trajectories, The RMSD values for the protein Cα, RNA, and ligand heavy atoms for 1μs for RTP, R1T, R2T, and R3T, The RMSF values for the protein amino acid residues for 1μs for RTP, R1T, R2T, and R3T, The ADME properties of RTP, R1T, R2T, and R3T are as predicted by SwissAdme webserver).

All data generated or analysed during this study are included in this published article (and its supplementary information files)

AUTHOR INFORMATION

Corresponding Author

*Muhammad Arba. Faculty of Pharmacy, Universitas Halu Oleo, Kendari 93232, Indonesia. Email: muh.arba@uho.ac.id

*Chun Wu. Department of Molecular & Cellular Biosciences, College of Science and Mathematics, Rowan University, Glassboro, New Jersey 08028, United States. Email: wuc@rowan.edu

Author Contributions

MA performed simulation, analyzed data, and wrote the manuscript. NP developed the ligand force field. STW, DJB, KRH, PML, and AT performed simulation. CW designed the work, analyzed data, and supervised the work. All authors approved the manuscript.

ACKNOWLEDGMENTS

MA and STW acknowledged the World Class Professor 2021 and Penelitian Dasar and Master Thesis Grants, respectively, from the Ministry of Education, Culture, Research and Technology Republic of Indonesia. CW thanks the support from the National Science Foundation of USA under Grants NSF RUI-1904797/ACI-1429467 and XSEDE MCB 170088.

Conflicts of interest/Competing interests

Authors declare no conflict of interest

Availability of data and material

All data included in this submission

REFERENCES

1. Mulangu, S., et al., *A Randomized, Controlled Trial of Ebola Virus Disease Therapeutics.* New England Journal of Medicine, 2019. **381**(24): p. 2293-2303.
2. Warren, T.K., et al., *Therapeutic efficacy of the small molecule GS-5734 against Ebola virus in rhesus monkeys.* Nature, 2016. **531**(7594): p. 381-385.
3. Sheahan, T.P., et al., *Broad-spectrum antiviral GS-5734 inhibits both epidemic and zoonotic coronaviruses.* Science Translational Medicine, 2017. **9**(396): p. eaal3653.
4. de Wit, E., et al., *Prophylactic and therapeutic remdesivir (GS-5734) treatment in the rhesus macaque model of MERS-CoV infection.* Proceedings of the National Academy of Sciences, 2020. **117**(12): p. 6771.
5. Consortium, W.s.t., *Repurposed Antiviral Drugs for Covid-19 — Interim WHO Solidarity Trial Results.* 2020.
6. Santoro, M.G. and E. Carafoli, *Remdesivir: From Ebola to COVID-19.* Biochemical and Biophysical Research Communications, 2020.

7. Wang, Y., et al., *Remdesivir in adults with severe COVID-19: a randomised, double-blind, placebo-controlled, multicentre trial.* The Lancet, 2020. **395**(10236): p. 1569-1578.
8. Gordon, C.J., et al., *The antiviral compound remdesivir potently inhibits RNA-dependent RNA polymerase from Middle East respiratory syndrome coronavirus.* Journal of Biological Chemistry, 2020. **295**(15): p. 4773-4779.
9. Wu, J., et al., *Remdesivir overcomes the S861 roadblock in SARS-CoV-2 polymerase elongation complex.* Cell Reports, 2021. **37**(4).
10. Gao, Y., et al., *Structure of the RNA-dependent RNA polymerase from COVID-19 virus.* Science (New York, N.Y.), 2020. **368**(6492): p. 779-782.
11. Yin, W., et al., *Structural basis for inhibition of the RNA-dependent RNA polymerase from SARS-CoV-2 by remdesivir.* Science, 2020. **368**(6498): p. 1499.
12. Gong, P., *Within and Beyond the Nucleotide Addition Cycle of Viral RNA-dependent RNA Polymerases.* Frontiers in Molecular Biosciences, 2022. **8**.
13. Shu, B. and P. Gong, *Structural basis of viral RNA-dependent RNA polymerase catalysis and translocation.* Proceedings of the National Academy of Sciences, 2016. **113**(28): p. E4005.
14. Bravo, J.P.K., et al., *Remdesivir is a delayed translocation inhibitor of SARS-CoV-2 replication.* (1097-4164 (Electronic)).
15. Brueckner, F., J. Ortiz, and P. Cramer, *A movie of the RNA polymerase nucleotide addition cycle.* Current Opinion in Structural Biology, 2009. **19**(3): p. 294-299.
16. Wang, D., et al., *Structural Basis of Transcription: Role of the Trigger Loop in Substrate Specificity and Catalysis.* Cell, 2006. **127**(5): p. 941-954.
17. Romero, M.E., et al., *Probing remdesivir nucleotide analogue insertion to SARS-CoV-2 RNA dependent RNA polymerase in viral replication.* Molecular Systems Design & Engineering, 2021. **6**(11): p. 888-902.
18. Arba, M., et al., *Mechanistic insight on the remdesivir binding to RNA-Dependent RNA polymerase (RdRp) of SARS-cov-2.* Computers in Biology and Medicine, 2021. **129**: p. 104156.
19. Madhavi Sastry, G., et al., *Protein and ligand preparation: parameters, protocols, and influence on virtual screening enrichments.* Journal of Computer-Aided Molecular Design, 2013. **27**(3): p. 221-234.
20. *CombiGlide*, in *3.3*. 2014, Schrodinger, LLC: New York, NY.
21. Bayly, C.I., et al., *A well-behaved electrostatic potential based method using charge restraints for deriving atomic charges: the RESP model.* The Journal of Physical Chemistry, 1993. **97**(40): p. 10269-10280.
22. Cornell, W.D., et al., *A Second Generation Force Field for the Simulation of Proteins, Nucleic Acids, and Organic Molecules.* Journal of the American Chemical Society, 1995. **117**(19): p. 5179-5197.
23. Meagher, K.L., L.T. Redman, and H.A. Carlson, *Development of polyphosphate parameters for use with the AMBER force field.* Journal of Computational Chemistry, 2003. **24**(9): p. 1016-1025.
24. Wang, J., et al., *Development and testing of a general amber force field.* Journal of Computational Chemistry, 2004. **25**(9): p. 1157-1174.
25. Case, D.A., et al., *The Amber biomolecular simulation programs.* Journal of Computational Chemistry, 2005. **26**(16): p. 1668-1688.

26. Maier, J.A., et al., *ff14SB: Improving the Accuracy of Protein Side Chain and Backbone Parameters from ff99SB.* Journal of Chemical Theory and Computation, 2015. **11**(8): p. 3696-3713.
27. Zgarbová, M., et al., *Refinement of the Cornell et al. Nucleic Acids Force Field Based on Reference Quantum Chemical Calculations of Glycosidic Torsion Profiles.* Journal of Chemical Theory and Computation, 2011. **7**(9): p. 2886-2902.
28. Banáš, P., et al., *Performance of Molecular Mechanics Force Fields for RNA Simulations: Stability of UUCG and GNRA Hairpins.* Journal of Chemical Theory and Computation, 2010. **6**(12): p. 3836-3849.
29. Arba, M., et al., *Mechanistic insight on the remdesivir binding to RNA-Dependent RNA polymerase (RdRp) of SARS-cov-2.* Computers in Biology and Medicine, 2021. **129**.
30. Mulholland, K., et al., *Three-Dimensional Structure of RNA Monomeric G-Quadruplex Containing ALS and FTD Related G4C2 Repeat and Its Binding with TMPyP4 Probed by Homology Modeling based on Experimental Constraints and Molecular Dynamics Simulations.* ACS Chemical Neuroscience, 2020. **11**(1): p. 57-75.
31. Sullivan, H.-J., B. Chen, and C. Wu, *A molecular dynamics study on the binding of an anti-cancer DNA G-quadruplex stabilizer, CX-5461, to human telomeric, cKIT-1, and c-Myc G-quadruplexes and a DNA duplex.* Journal of Chemical Information and Modeling, 2020. **80**(10): p. 5203-5224.
32. Chen, B., et al., *To probe the binding pathway of a selective compound (D089-0563) to c-MYC Pu24 G-quadruplex using free ligand binding simulations and Markov state model analysis.* Physical Chemistry Chemical Physics, 2020.
33. Machireddy, B., H.J. Sullivan, and C. Wu, *Binding of BRACO19 to a Telomeric G-Quadruplex DNA Probed by All-Atom Molecular Dynamics Simulations with Explicit Solvent.* Molecules, 2019. **24**(6).
34. Sullivan, H.J., et al., *Binding of Telomestatin, TMPyP4, BSU6037, and BRACO19 to a Telomeric G-Quadruplex-Duplex Hybrid Probed by All-Atom Molecular Dynamics Simulations with Explicit Solvent.* Acs Omega, 2018. **3**(11): p. 14788-14806.
35. Shen, Z., et al., *Binding of Anticancer Drug Daunomycin to a TGGGGT G-Quadruplex DNA Probed by All-Atom Molecular Dynamics Simulations: Additional Pure Groove Binding Mode and Implications on Designing More Selective G-Quadruplex Ligands.* Journal of Molecular Modeling, 2017(23): p. 256.
36. Machireddy, B., et al., *Probing the Binding Pathway of BRACO19 to a Parallel-Stranded Human Telomeric G-Quadruplex Using Molecular Dynamics Binding Simulation with AMBER DNA OL15 and Ligand GAFF2 Force Fields.* Journal of Chemical Information and Modeling, 2017. **57**(11): p. 2846-2864.
37. Mulholland, K. and C. Wu, *Binding of Telomestatin to a Telomeric G-Quadruplex DNA Probed by All-Atom Molecular Dynamics Simulations with Explicit Solvent.* Journal of Chemical Information and Modeling, 2016. **56**(10): p. 2093−2102.
38. Darden, T., D. York, and L. Pedersen, *Particle mesh Ewald: An N·log(N) method for Ewald sums in large systems.* The Journal of Chemical Physics, 1993. **98**(12): p. 10089-10092.
39. Stuart, S.J., R. Zhou, and B.J. Berne, *Molecular dynamics with multiple time scales: The selection of efficient reference system propagators.* The Journal of Chemical Physics, 1996. **105**(4): p. 1426-1436.

40. Roe, D.R. and T.E. Cheatham, *PTRAJ and CPPTRAJ: Software for Processing and Analysis of Molecular Dynamics Trajectory Data.* Journal of Chemical Theory and Computation, 2013. **9**(7): p. 3084-3095.
41. Shao, J., et al., *Clustering Molecular Dynamics Trajectories: 1. Characterizing the Performance of Different Clustering Algorithms.* Journal of Chemical Theory and Computation, 2007. **3**(6): p. 2312-2334.
42. Kollman, P.A., et al., *Calculating Structures and Free Energies of Complex Molecules: Combining Molecular Mechanics and Continuum Models.* Accounts of Chemical Research, 2000. **33**(12): p. 889-897.
43. Daina, A., O. Michielin, and V. Zoete, *SwissADME: a free web tool to evaluate pharmacokinetics, drug-likeness and medicinal chemistry friendliness of small molecules.* Scientific Reports, 2017. **7**(1): p. 42717.
44. El-Gebali, S., et al., *The Pfam protein families database in 2019.* Nucleic Acids Res, 2019. **47**(D1): p. D427-D432.
45. Katoh, K., J. Rozewicki, and K.D. Yamada, *MAFFT online service: multiple sequence alignment, interactive sequence choice and visualization.* Briefings in Bioinformatics, 2019. **20**(4): p. 1160-1166.
46. Corpet, F., *MULTIPLE SEQUENCE ALIGNMENT WITH HIERARCHICAL-CLUSTERING.* Nucleic Acids Research, 1988. **16**(22): p. 10881-10890.
47. Aranda, J. and M. Orozco, *RNA-Dependent RNA Polymerase From SARS-CoV-2. Mechanism Of Reaction And Inhibition By Remdesivir.* bioRxiv, 2020: p. 2020.06.21.163592.
48. Genna, V., et al., *A Self-Activated Mechanism for Nucleic Acid Polymerization Catalyzed by DNA/RNA Polymerases.* Journal of the American Chemical Society, 2016. **138**(44): p. 14592-14598.
49. Rungrotmongkol, T., A.J. Mulholland, and S. Hannongbua, *QM/MM simulations indicate that Asp185 is the likely catalytic base in the enzymatic reaction of HIV-1 reverse transcriptase.* Medchemcomm, 2014. **5**(5): p. 593-596.
50. Gong, P. and B. Peersen Olve, *Structural basis for active site closure by the poliovirus RNA-dependent RNA polymerase.* Proceedings of the National Academy of Sciences, 2010. **107**(52): p. 22505-22510.
51. Zamyatkin, D.F., et al., *Structural Insights into Mechanisms of Catalysis and Inhibition in Norwalk Virus Polymerase *.* Journal of Biological Chemistry, 2008. **283**(12): p. 7705-7712.
52. Jiang, Y., W. Yin, and H.E. Xu, *RNA-dependent RNA polymerase: Structure, mechanism, and drug discovery for COVID-19.* Biochemical and Biophysical Research Communications, 2020.
53. Wang, Q., et al., *Structural Basis for RNA Replication by the SARS-CoV-2 Polymerase.* Cell, 2020. **182**(2): p. 417-428.e13.
54. Gao, Y., et al., *Structure of the RNA-dependent RNA polymerase from COVID-19 virus.* Science, 2020. **368**(6492): p. 779.
55. Gordon, C.J., et al., *Remdesivir is a direct-acting antiviral that inhibits RNA-dependent RNA polymerase from severe acute respiratory syndrome coronavirus 2 with high potency.* The Journal of biological chemistry, 2020. **295**(20): p. 6785-6797.
56. Tchesnokov, E.P., et al., *Mechanism of Inhibition of Ebola Virus RNA-Dependent RNA Polymerase by Remdesivir.* Viruses-Basel, 2019. **11**(4).

57. Tchesnokov, E.P., et al., *Template-dependent inhibition of coronavirus RNA-dependent RNA polymerase by remdesivir reveals a second mechanism of action.* The Journal of biological chemistry, 2020. **295**(47): p. 16156-16165.
58. Tchesnokov, E.P., et al., *Delayed chain termination protects the anti-hepatitis B virus drug entecavir from excision by HIV-1 reverse transcriptase.* The Journal of biological chemistry, 2008. **283**(49): p. 34218-34228.
59. Sgrignani, J. and A. Magistrato, *The Structural Role of Mg2+ Ions in a Class I RNA Polymerase Ribozyme: A Molecular Simulation Study.* The Journal of Physical Chemistry B, 2012. **116**(7): p. 2259-2268.
60. Hillen, H.S., et al., *Structure of replicating SARS-CoV-2 polymerase.* Nature, 2020. **584**: p. 154-156.
61. Nguyen, H.L., et al., *Remdesivir Strongly Binds to Both RNA-Dependent RNA Polymerase and Main Protease of SARS-CoV-2: Evidence from Molecular Simulations.* The Journal of Physical Chemistry B, 2020. **124**(50): p. 11337-11348.
62. Cavasotto, C.N., N.S. Adler, and M.G. Aucar, *Quantum Chemical Approaches in Structure-Based Virtual Screening and Lead Optimization.* Frontiers in chemistry, 2018. **6**: p. 188-188.
63. Picarazzi, F., et al., *Targeting the RdRp of Emerging RNA Viruses: The Structure-Based Drug Design Challenge.* Molecules, 2020. **25**(23).
64. Carvalho, A.T.P., P.A. Fernandes, and M.J. Ramos, *The Catalytic Mechanism of RNA Polymerase II.* Journal of Chemical Theory and Computation, 2011. **7**(4): p. 1177-1188.
65. Homeyer, N. and H. Gohlke, *Free Energy Calculations by the Molecular Mechanics Poisson−Boltzmann Surface Area Method.* Molecular Informatics, 2012. **31**(2): p. 114-122.
66. Foloppe, N. and R. Hubbard, *Towards Predictive Ligand Design With Free-Energy Based Computational Methods?* Current Medicinal Chemistry, 2006. **13**(29): p. 3583-3608.